Available online at www.sciencedirect.com
ScienceDirect
Journal of Power Sources 179 (2008) 113–120
JOURNAL OF POWER SOURCES
www.elsevier.com/locate/jpowsour

# Portable power production from methanol in an integrated thermoeletric/microreactor system

A.M. Karim, J.A. Federici, D.G. Vlachos *

*Department of Chemical Engineering, Center for Catalytic Science and Technology, and Center for Composite Materials, University of Delaware, Newark, DE 19716, United States*

Received 22 November 2007; received in revised form 20 December 2007; accepted 31 December 2007
Available online 17 January 2008

**Abstract**

Catalytic self-ignition of methanol over platinum supported on anodized alumina in a microburner is demonstrated. The effects of air flow rate and air/methanol ratio on the system start-up time and steady state temperature have been studied. The air flow rate strongly affects the system start-up time. However, at the same flow rate, the start-up time is not affected by the air/methanol ratio over the range studied. Computational fluid dynamics simulations confirm these experimental findings. It is proposed that high flow rates and relatively lower fuel content can lead to attaining steady state faster with minimal fuel utilization. Transient axial temperature profiles showed that the hot spot of the reaction started at the inlet of the burner and did not shift downstream with time under most reaction conditions. The burner effective thermal conductivity was increased using copper thermal spreaders on the burner outer walls, allowing for thermally uniform walls. The uniform temperature profile allowed for optimal integration of the microburner with a thermoelectric device. The integrated microburner/thermoelectric device was shown to self-start from room temperature. The maximum power generated with the thermoelectric was 0.65 W and the maximum thermal efficiency was 1.1%.


*Keywords:* Methanol; Portable power generation; Microreactor; Thermoelectric; Platinum; Ignition

## 1. Introduction

There is an increasing demand for portable power supply using higher energy density systems and for longer operational time between recharges [1]. Unfortunately, battery technology has not kept pace with the increasing power demand for portable electronics, which forced manufacturers to introduce power-down options to prolong the battery operational time. Similarly, the military has also been interested in portable power sources for long-duration missions where portable electronics are increasingly being used [2]. Hydrocarbons possess high gravimetric and volumetric energy density compared to batteries. For instance, the energy density of diesel fuel (12 kW h $kg^{-1}$) and methanol (5.6 kW h $kg^{-1}$) are each at least an order of magnitude greater than that of lithium-ion batteries (0.2 kW h $kg^{-1}$) [3,4]. In recent years, new approaches, ranging from direct methanol fuel cells [5,6], to reformed hydrogen fuel cells [2–4,7], to (thermal to electric energy) devices integrated with microburners [8–12] have been investigated as alternative technologies that generate electric power from fuels.

Proton exchange membrane (PEM) fuel cell systems operating on pure hydrogen possess high energy density and exhibit efficiencies as high as 70%. Hydrogen production from fuels currently appears as the only viable option due to the low volumetric energy density of hydrogen and the difficulty and safety issues associated with its storage. Unfortunately, the integration of a fuel reformer, combustor and carbon monoxide conversion and cleaning units (shift reactors plus preferential oxidation reactor or a separation unit) with a fuel cell severely degrades the overall system performance and make a portable system quite complicated (due to multiple fuel streams and different operating temperatures of various systems). Holladay et al. reported obtaining 100 mW maximum electrical output from a mesoscale fuel cell operating on pure hydrogen. Based on the reported $H_2$ flow rate and the lower heating value of $H_2$, we calculated the thermal efficiency of the fuel cell to be about 33%. However, the efficiency of the fuel cell dropped to 16.3% when integrated with the methanol reformer and com-

* Corresponding author. Tel.: +1 302 831 2830.
*E-mail address:* vlachos@udel.edu (D.G. Vlachos).

0378-7753/$ – see front matter © 2008 Elsevier B.V. All rights reserved.
doi:10.1016/j.jpowsour.2007.12.119

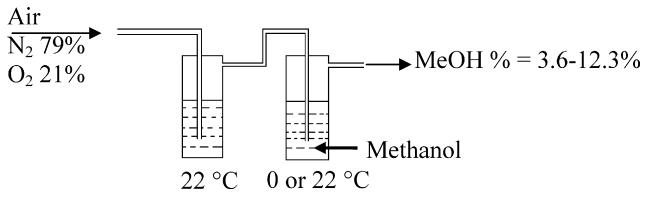


Fig. 1. Methanol delivery system.

bustor and the maximum electrical power produced by the integrated system was 23 mW. The authors attributed the loss in performance to the operation with reformate ($H_2$, $CO_2$ and CO) instead of pure $H_2$ [4]. The highest thermal efficiency reported for their integrated reformer/combustor without the fuel cell was 9% [3]. Therefore, we estimate the total efficiency of the integrated reformer/combustor/fuel cell system to be about $16.3\% \times 9\% = 1.5\%$. A thermoelectric device integrated with a microburner clearly offers a simpler design over a reformed fuel cell system at a comparable efficiency, as was shown by Federici et al. [9].

In our earlier work, we found that hydrogen self-ignites on platinum (Pt) nanoparticles dispersed on anodized alumina wafers. This feature simplifies start-up since no other ignition sources need to be integrated. Hydrogen can also be used to ignite hydrocarbon fuels [13]. However, self-ignition of small hydrocarbons (alkanes up to butane) has not been feasible due to the difficulty in activating the C–H bond cleavage. Methanol has been shown to self-ignite catalytically on supported Pt and Pd catalysts [14–16]. Self-ignition of methanol has also been shown to occur over $Pt/Al_2O_3$ even when the burner was kept at 0 °C [16].

In this work, we study the catalytic ignition of lean methanol/air mixtures over Pt catalyst dispersed on anodized alumina wafers embedded in a microburner. Our focus on the simplest alcohol has in part been motivated from the recent interest in oxygenated fuels, some of which could be produced from bio-renewable sources, and its inherent advantage in terms of being liquid at room temperature but with a relatively high vapor pressure. The effects of air flow rate and air/methanol ratio on the start-up time and steady state temperature have been studied in order to develop strategies for optimal start-up. Computational fluid dynamics (CFD) simulations are carried out to confirm the experimental findings. Finally, control of temperature profiles is demonstrated and the efficiency of integrated self-starting, microburner-thermoelectric devices is estimated from experimental data.

## 2. Experimental

### 2.1. Microburner setup

Fig. 1 shows the methanol/air mixing system. The air flows through two methanol bubblers where it gets enriched with methanol vapor. The first bubbler was held at room temperature while the second was held either at 0 °C or at room temperature.

Fig. 2 shows a schematic of the microburner design. The burner consists of two rectangular sheets of 0.79 mm thick 316-

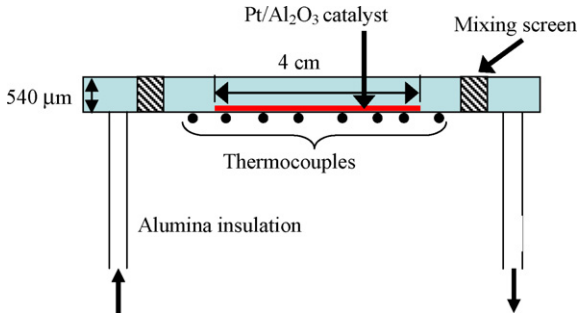


Fig. 2. Schematic of the burner design (side view).

alloy stainless steel, with a bolt pattern around the exterior. A thin (540 μm) gasket separates the two sheets to form a rectangular microchannel approximately 6 cm long by 1 cm wide. Stainless steel inlet and outlet tubes were welded to one of the exterior sheets. Fine metal screens were spot welded near the inlet and outlet of the channel in order to induce uniform flow over the microchannel. As in previous work [8], two copper thermal spreaders were used to change the effective thermal conductivity of the walls in order to facilitate axial heat transfer. In order to provide a uniform surface of the same dimensions of the thermoelectric, a secondary copper, thermal spreader was installed in experiments conducted with thermoelectrics.

An $Al_2O_3$ wafer, approximately 100 μm in thickness, has been inserted into the burner, which reduced the burner gap size to ~440 μm. Eight K-type thermocouples were placed on the outer wall of the burner to record the temperature profile. The temperature profile during ignition was monitored via Labview© software and National Instruments data acquisition board. The burner setup has been described in detail in previous work [8,9].

### 2.2. Catalyst preparation

The $Al_2O_3$ support was prepared by completely anodizing 100 μm-thick 1145 alloy aluminum foil to create thin alumina wafers that serve as high-surface area porous catalyst supports (approximately 100 μm thick). The foil is immersed in 0.3 M aqueous oxalic acid at a potential of 40 V for 48 h. The system is held at approximately 1–2 °C using an ice bath. The pore structure is semi-ordered with an average pore diameter of 50 nm and a surface area of approximately 14 $m^2\ g^{-1}$. The pores travel the thickness of the wafer.

The $Pt/Al_2O_3$ catalyst was prepared by wet impregnation, where the platinum was deposited by immersing the $Al_2O_3$ wafer in 0.007 M aqueous dihydrogen hexachloroplatinate(IV) with pH 3 (for optimal surface charge) for 3 h [17]. The $Al_2O_3$ wafers were then removed from the solution and dried overnight, and subsequently calcined in air at 500 °C for 3 h. Prior to reactivity measurements, the catalyst was reduced in 100 sccm 10% $H_2$ (balance He) at 300 °C for 3 h. The Pt weight loading was approximately 1 wt.% as determined by atomic absorption spectroscopy. The catalyst loading in the burner was between 75 and 85 mg.

### 2.3. Composition measurements

The exhaust gases were sampled with a gas-sampling valve, and the composition was monitored with a HP Series 6890 gas chromatograph (GC), using both a thermal conductivity detector and a flame ionization detector. As seen in Fig. 1, the air flows through two methanol bubblers where the incoming stream gets saturated with methanol at the low air flow rates as confirmed by the GC. However, at the higher flow rates the temperature of the bubbler drops due to the fast evaporation of methanol and it is not clear whether the incoming stream is saturated or not. The methanol mole fraction in the mixture varied from 3.6 to 12.3%. The fraction of methanol in the mixture was determined by back calculating the methanol percentage from the products composition assuming the total oxidation reaction stoichiometry (this is indeed the product distribution as the results show below). To verify this method, we later measured the methanol fraction in the inlet mixture directly and the composition was within 10% of the calculated.

A methanol mole fraction of 12.3% in the mixture is equivalent to stoichiometric oxygen to methanol ratio of 1.5. Therefore, all experiments were conducted under fuel lean conditions. The methanol conversion was calculated based on a carbon balance using the measured composition of carbon dioxide and methanol, if any, in the exhaust gases. The error in the total mass balance was lower than 10% in all experiments.

## 3. Results

### 3.1. Catalyst characterization

Scanning transmission electron microscopy (STEM) was performed on a JEOL 2010F FASTEM field emission gun scanning transmission electron microscope (STEM). The catalyst wafer used in the burner integrated with the thermoelectric was taken out of the burner for characterization. The catalyst wafer was used for about 60 h on stream with over 20 ignition and shut down cycles. No apparent catalyst deactivation was observed. No deactivation was seen in previous microreactor work involving longer runs and more adverse temperature conditions than the ones used herein [8]. The catalyst wafer was crushed into fine powder and dispersed in ethanol. A sample of the dispersed catalyst was dropped on a carbon coated copper TEM grid.

We used high angle annular dark field imaging (HAADF) in the STEM mode to enable detection of the smallest particles. Fig. 3 shows a representative STEM image of the spent catalyst. The Pt nanoparticles and the $Al_2O_3$ pores can be seen in the image as bright and dark areas, respectively. Over several images, we measured the particle size of more than 900 Pt nanoparticles. The corresponding particle size distribution is shown in Fig. 4. The Pt number average particle diameter ($N_{avg} = \sum_i n_i d_i / \sum_i n_i$, $d_i$ being the particle diameter and $n_i$ the number of particles) was 4.5 nm. However, the particle size distribution is broad with particles as large as 25 nm. The Pt dispersion was about 10% based on the mean surface diameter ($N_s = \sum_i n_i d_i^3 / \sum_i n_i d_i^2$) [18]. The low dispersion is due to sintering from operating at temperatures as high as 650 °C.

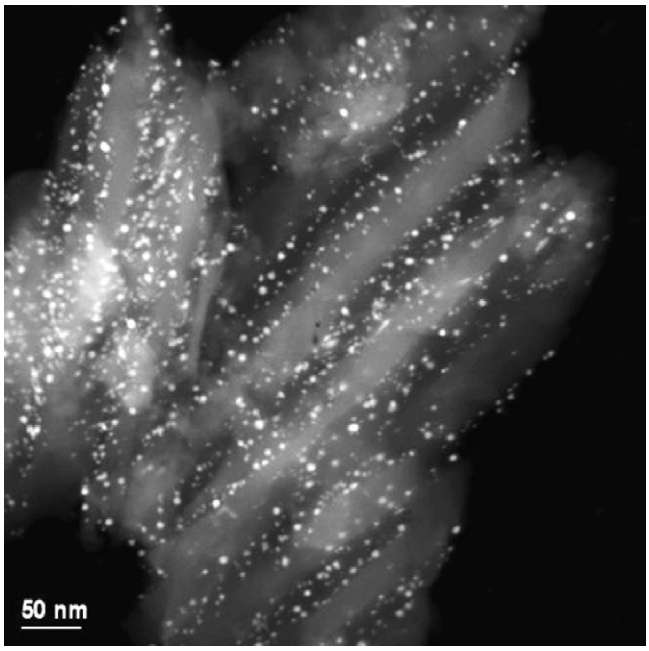


Fig. 3. STEM image of the spent catalyst (1 wt.% $Pt/Al_2O_3$).

However, despite the broad particle size distribution and low dispersion, ignition at room temperature was achieved under all conditions studied even after the catalyst has been on stream for 60 h.

### 3.2. Effect of flow rate and methanol mole fraction on temperature profiles

Figs. 5 and 6 show the transient temperature profiles during methanol ignition at 1000 sccm air flow rate and 10% methanol mole fraction in the mixture. The hot spot reached 100 °C within 10 s of start-up. The transient temperature profile at position 1 cm (see Fig. 5) was fitted to a first-order dynamics model, $a(1 - e^{-t/\tau})$, where $a$ is a normalizing factor, $t$ is time and $\tau$ is the time constant of the system. Accordingly, we find that the sys-

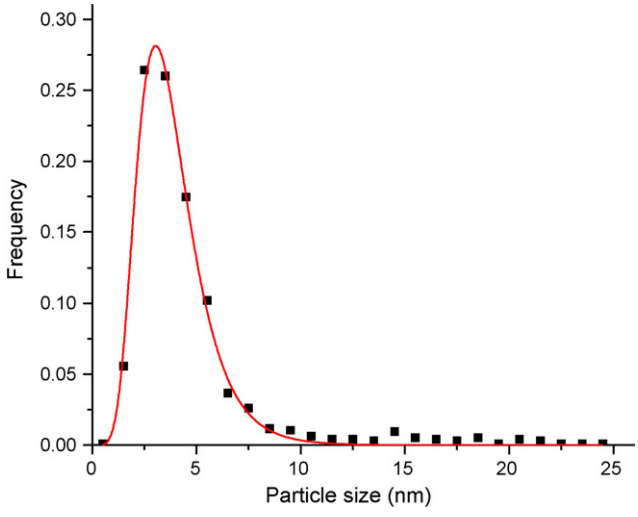


Fig. 4. Pt particle size distribution of the spent catalyst (1 wt.% $Pt/Al_2O_3$).

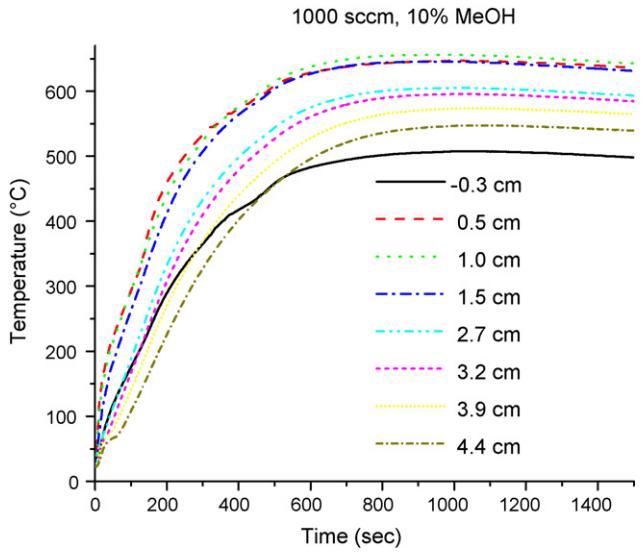


Fig. 5. Transient temperature profiles. Air flow rate 1000 sccm, 10% methanol in the mixture. Thermocouple positions stated with the catalyst starting at 0 cm.

tem reached 95% of the steady state temperature (at time = $3\tau$) in about 9 min. The location of the hot spot near the entrance of the catalytic region indicates very fast kinetics of methanol oxidation on Pt. The reaction products were analyzed at both approximately 60 s from starting the experiment and at steady state. Both conditions showed 100% methanol conversion to water and carbon dioxide.

Fig. 7 shows the steady state temperature profiles at different methanol mole fractions and air flow rates. At low methanol mole fractions, the temperature profiles are more uniform and the average temperature is much lower than at high methanol mole fractions. The hot spot was near the entrance (about 5 mm) of the catalytic region for all conditions with the exception of 1000 sccm air flow rate where the hot spot shifted slightly downstream. At all flow rates, the methanol conversion was >99% and the only products detected at steady state were water and carbon dioxide. During the first minute of starting the experiment, formaldehyde and methanol breakthrough were observed at low methanol mole fractions. No methanol breakthrough was

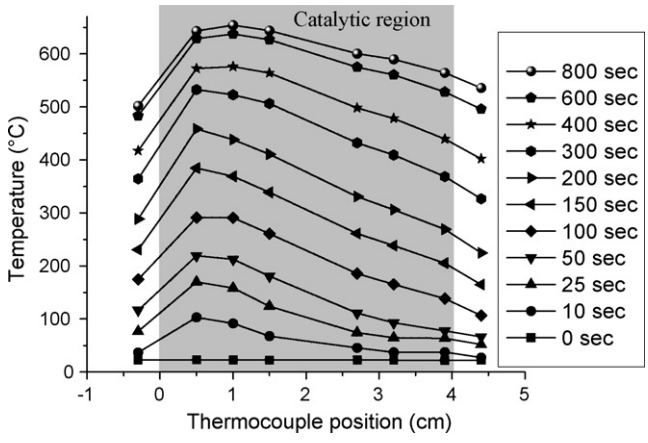


Fig. 6. Transient temperature profiles. Air flow rate = 1000 sccm, 10% methanol the mixture.

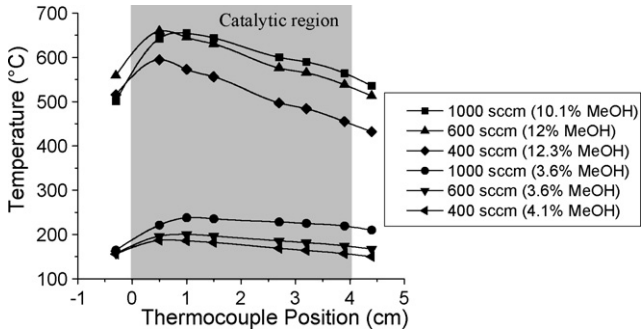


Fig. 7. Effect of air flow rate and methanol mole fraction in the mixture on steady state temperature profiles.

detected at 60 s at higher methanol mole fractions. This is most probably due to the higher temperatures reached with higher methanol mole fraction in the feed.

### 3.3. Effect of flow rate and methanol mole fraction on start-up

The steady state temperatures vary with varying flow rate and methanol composition. In order to compare the system start-up time for different conditions, the dimensionless temperature ($T/T_{ss}$) was introduced, as the temperature $T$ at position of 1 cm divided by the steady state temperature, $T_{ss}$, at the same position.

At the same air flow rate, higher methanol mole fraction resulted in a faster heating rate; however, the steady state temperature was also higher. Therefore, as shown in Fig. 8, the time it takes the system to reach steady state (start-up time) is weakly affected by the air/methanol ratio. The air flow rate on the other hand, highly affects the start-up time, as shown in Fig. 8. At higher air flow rate, the rate of heat release by methanol oxidation increases, and therefore, the temperature increases at a faster rate. Jiang et al. [16] have reported similar results on the effect of flow rate at a methanol mole fraction of 11.5%.

The above results can be rationalized by simplifying the problem to a continuous stirred tank reactor and solving the time

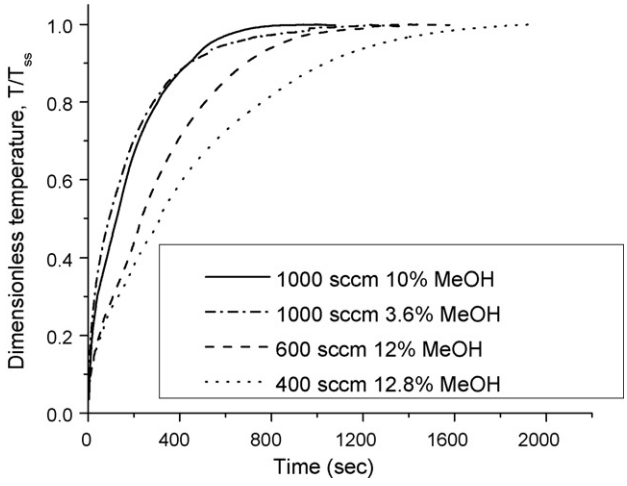


Fig. 8. Effect of methanol mole fraction in the mixture on system start-up in terms of dimensionless temperature $T/T_{ss}$ at 1 cm (from the catalyst entrance) vs. time.

dependent energy balance for an ideal gas (assuming complete fuel conversion). Eq. (1) gives the temperature versus time in terms of the total flow rate $\dot{V}_{in}$, initial temperature $T_i$, methanol mole fraction $y_{MeOH}$, mass of the system $m$ (this is mainly comprised of the solid walls in a microchemical system), heat capacity of the system $C_p$, heat capacity of the fluid, $C_{Pf}$, density of the fluid at the inlet, $\rho_{in}$, heat of reaction $\Delta H$, heat loss coefficient $h$, inlet methanol concentration $C_{in}$, and surface area of the system available for heat transfer $A$ (the term $\rho_{in}C_{Pf}$ is assumed to be independent of temperature, a common assumption in the combustion literature; a reference temperature for the gas enthalpy and heat of reaction of 298 K is chosen).

$$T = \left\{ T_i - \frac{\dot{V}_{in}[\rho_{in}C_{Pf}T_{in} + \Delta H\, y_{MeOH}C_{in}] + T_{amb}hA}{hA + \dot{V}_{in}\rho_{in}C_{Pf}} \right\} e^{-t/\tau} + \frac{\dot{V}_{in}[\rho_{in}C_{Pf}T_{in} + \Delta H\, y_{MeOH}C_{in}] + T_{amb}hA}{hA + \dot{V}_{in}\rho_{in}C_{Pf}} \quad (1)$$

The characteristic time scale of the system is given by

$$\tau = \frac{mC_p}{hA + \dot{V}(\rho C_P)_{out}} \quad (2)$$

The time constant of the system, $\tau$, does not depend on the methanol mole fraction. However, $\tau$ is inversely proportional to the total flow rate. The above expression for $\tau$ confirms the observed experimental results, where the system start-up was only affected by the air flow rate and insensitive to the methanol mole fraction. Two-dimensional (in space), time dependent CFD simulations, summarized in Appendix A, indicate that this dependence on flow rate and independence of mixture composition is probably a generic behavior of catalytic combustion.

### 3.4. Effect of increasing the burner wall thermal conductivity

In order to achieve uniform temperature profiles, two copper thermal spreaders were installed on both sides of the burner to increase the effective axial thermal conductivity [9]. Each copper spreader was 5 cm long × 1 cm wide × 1.8 cm thick and weighed about 3.5 g. Fig. 9 shows the steady state temperature profiles with the copper thermal spreaders installed. The higher effective axial thermal conductivity resulted in a uniform temperature profile.

The copper thermal spreaders also slowed down the system start-up, as shown in Fig. 10. The slower system start-up is due to the increase in thermal conductivity and mass of the system. The increased mass of the system has a direct effect on the time constant for start-up, as seen from Eq. (1). The thermal conductivity on the other hand, affects the time constant indirectly by modifying the temperature profile, and in turn the local rate of heat release. As methanol and air enter the burner, the heat released by combustion is absorbed by the burner wall and causes a localized temperature rise. The burner having low axial thermal conductivity (without copper thermal spreaders) conducts heat slowly in the axial direction, and therefore, the reaction rate at the hot spot increases faster, leading to faster system start-up. On the other hand, the burner with a higher effective axial thermal conductivity conducts heat faster in the axial direction and in turn the reaction rate is slower due to lower temperatures [19]. The slower reaction rate and the increased mass result in a slower system start-up.

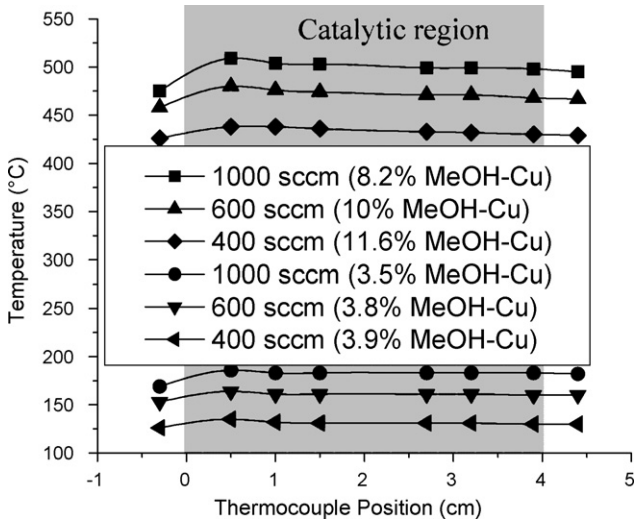


Fig. 9. Steady state temperature profiles with copper thermal spreaders installed on the outer walls of the burner.

### 3.5. Microburner integration with a thermoelectric device

The thermoelectric module used was Model HZ-2 from Hi-Z Technology, Inc. (San Diego, CA). The device is approximately 2.9 cm wide × 2.9 cm long × 0.5 cm thick, and weighs 13.5 g. Two pieces of 1 mm thick aluminum nitride electrical insulating wafers were placed between the secondary thermal spreader and the thermoelectric device to prevent electrical shorting between thermoelectric elements. To ensure good thermal contact, thermal grease obtained from Hi-Z Technologies was placed between the thermal spreaders, electrical insulating wafers, and thermoelectric module. A finned copper heat sink, CoolWaveCPUCooler from Spire, was placed on top of the thermoelectric module to enhance convective cooling efficiency. To further ensure thermal contact, the entire microburner/thermal spreader/thermoelectric/heat sink stack was placed under com-

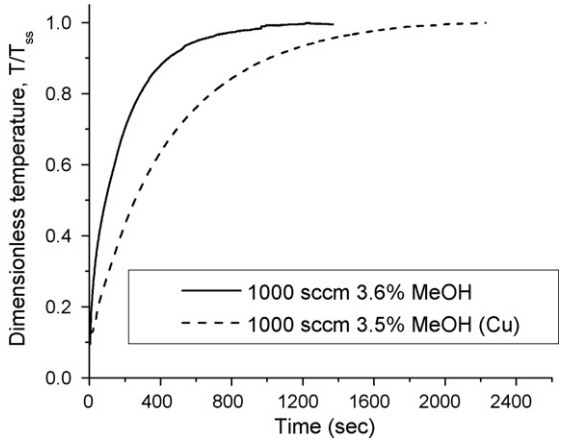


Fig. 10. Effect of thermal spreaders on system start-up.

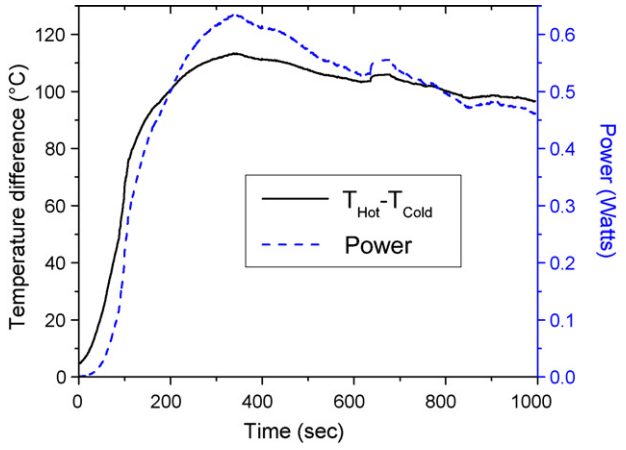


Fig. 11. Thermoelectric transient temperature difference and power vs. time. Air flow rate = 2000 sccm, 9% methanol in air, $\Delta S = 0.032\ \mathrm{V\,K^{-1}}$.

pressive force using a conventional C-clamp. It was shown in previous work that this compressive force has a positive effect on the power generated from the system [9].

Fig. 11 shows the temperature difference between the hot and cold sides of the thermoelectric as a function of time. Also shown is the calculated power using

$$P = R_{\mathrm{load}}\left(\frac{\Delta S\,\Delta T}{R_{\mathrm{load}} + R_{\mathrm{int}}}\right)^2 \tag{3}$$

where $\Delta S$ is the difference between the Seebeck coefficients of the two materials of the thermoelectric and $\Delta T$ is the temperature difference between the hot and cold sides. The load resistance ($R_{\mathrm{load}}$) was matched to the thermoelectric's internal resistance ($R_{\mathrm{int}} = 5.3\ \Omega$) to calculate the maximum power. The open circuit voltage of the thermoelectric was measured at steady state under different air flow rates and methanol mole fractions. For the different conditions, $\Delta S$ was calculated from the following equation $V = \Delta S \times \Delta T$, where $V$ is the open circuit voltage, and we used the average $\Delta S$ ($0.032\ \mathrm{V\,K^{-1}}$) to calculate the power output in Fig. 11.

As shown in Fig. 11, the temperature difference between the hot and cold sides increases with time until it reaches a maximum around 6 min where the output power is maximum (0.65 W). Then the temperature difference and output power start decreasing, and they reach steady state around 15 min. The reason for the maximum in temperature difference, and therefore in power, is the slow heat removal from the cold side. As the system starts, the burner starts heating up the hot side of the thermoelectric and its temperature increases. However, heat is also conducted to the cold side of the thermoelectric where it is dissipated and removed by the heat sink. This creates a lag time between the cold side transient temperature profile relative to the hot side (data not shown). Hence, as the hot side temperature reaches steady state, the cold side temperature keeps increasing, resulting in a maximum in the temperature difference and output power. The efficiency was calculated using

$$\text{efficiency}\ (\%) = \frac{P_{\mathrm{gen}}}{\dot{m}\,\Delta H} \times 100 \tag{4}$$

where $P_{\mathrm{gen}}$ is the maximum power generated, $\dot{m}$ is the mass flow rate of methanol, and $\Delta H$ is the heat of combustion for methanol (lower heating value). The maximum efficiency estimated from the data was 1.1%.

The steady state, generated power for the methanol system was slightly higher than that of previous work with hydrogen and propane [9]. In Fig. 11, the system generates approximately 450 mW with a temperature differential of about 100 °C. In contrast, the highest power output from the previous study was approximately 420 mW at a higher temperature differential of 110 °C. This is most likely due to the fact that the thermoelectrics were observed to have different Seebeck coefficient values, as the module used in this study had a lower operating time. Also, more compressive force may have been applied to the methanol system, which was shown to substantially increase the heat transfer to the thermoelectric, increasing the apparent difference in Seebeck coefficients.

With respect to other integrated, portable burner/thermoelectric systems utilizing liquid or easy to liquefy fuels, Yoshida et al. has demonstrated power generation using butane with a Laval nozzle ejection system [20]. However, they required the use of resistive heaters to start-up the system and were unable to sustain catalytic butane combustion autothermally, i.e., without an external heat supply.

The efficiency of the integrated microburner/thermoelectric system still needs to be improved in order to become a competitive alternative to batteries in low power portable applications. However, the integrated system was not optimized. Yet, its major advantage is its simplicity as it integrates only a few parts. Some strategies for increasing its thermal efficiency include: (1) use of a second thermoelectric (e.g., on the other side of the microburner) to utilize more effectively the heat generated from the microburner. (2) Heat recovery from the exhaust. (3) Heat removal from the cold side of the thermoelectric by the reactants through a micro-heat exchanger. This approach will pre-heat the reactants (a desirable phenomenon) while increasing the temperature difference between the hold and cold sides of the thermoelectric.

## 4. Conclusions

Catalytic self-ignition of methanol over Pt nanoparticles dispersed on an anodized alumina wafer in a microburner was demonstrated. The microburner was integrated with a thermoelectric device and the system was also shown to be self-starting from room temperature at all air flow rates and air/methanol ratios studied. The system start-up time was highly affected by the air flow rate and the thermal mass of the system but nearly independent of the mixture composition. The system reached steady state faster at higher air flow rates. These findings should be fairly generic as simple theoretical analysis and CFD simulations indicate. It is thus proposed that high flow rates and relatively lower fuel content should be used in order to reach steady state faster with minimal fuel utilization. The maximum power generated with the thermoelectric was 0.65 W and the maximum thermal efficiency was 1.1%. This is the highest reported integrated thermoelectric/microreactor efficiency

reported using a liquid fuel. The efficiency we report is also close to that of an integrated fuel reformer, combustor, fuel cell system [4]. Considering the simplicity of the thermoelectric/microreactor system, it is probably a better alternative for low power (∼1 W) production for portable devices.


## Acknowledgments

The research was sponsored by the Army Research Laboratory and was accomplished under Cooperative Agreement Number W911NF-06-2-0011. The views and conclusions contained in this document are those of the authors and should not be interpreted as representing the official policies, either expressed or implied, of the Army Research Laboratory or the U.S. Government. The U.S. Government is authorized to reproduce and distribute reprints for Government purposes notwithstanding any copyright notation heron. The authors would like to thank Dr. Eric. D. Wetzel and Dr. Bruce R. Geil from the Army Research Laboratory for useful discussions.


## Appendix A. Computational fluid dynamics (CFD) simulations for the effect of flow rate and mixture composition on start-up time

In order to verify the experimental findings and assess the insights gained from the simple theoretical analysis presented above, CFD simulations were carried out. The microreactor is modeled as two parallel plates of infinite width and 793 μm (1/32″) thickness, as done in previous work [8]. The combustion chamber has a gap size of 400 μm and is 1 cm long. Premixed, methanol/air mixtures are sent to the reactor with a uniform flow velocity at ambient temperature (300 K) into the combustion chamber.

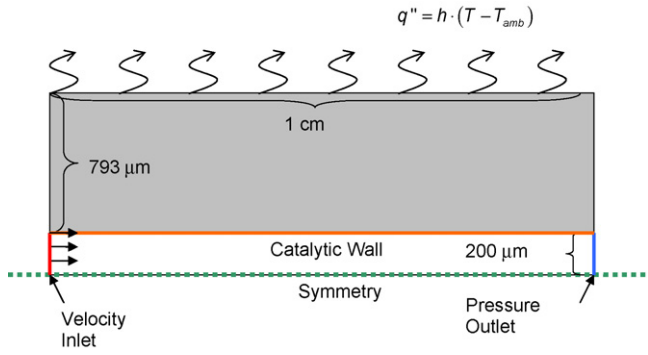


Fig. A.1. Schematic of computational fluid dynamics (CFD) geometry and boundary conditions used.

The CFD package Fluent 6.2 is used to solve the spatially 2D time dependent continuity, momentum, species, and energy equations using a finite volume method. The mesh used to perform these calculations was generated in the commercial package Gambit and contained 101 and 100 uniformly spaced

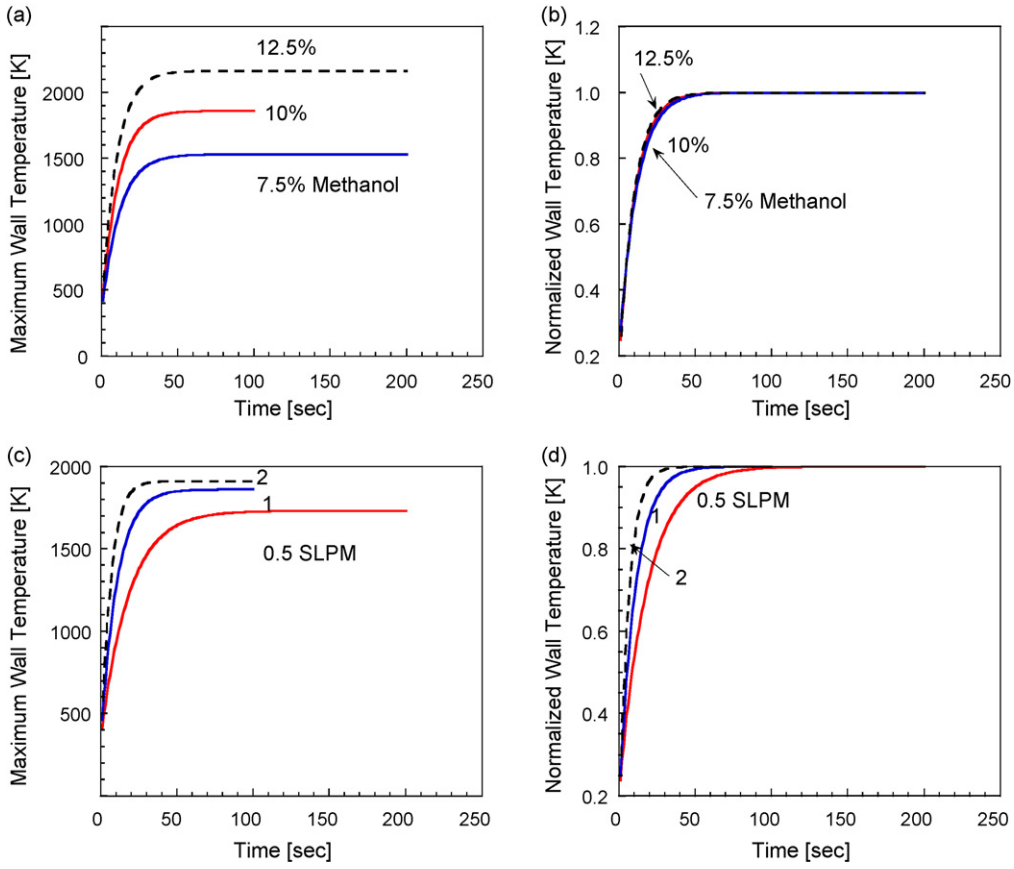


Fig. A.2. Maximum wall temperature vs. time for varying composition (a) and flow rate (c). The corresponding normalized transient graphs are labeled as (b) and (d), respectively. In all cases, the wall thermal conductivity is 30 W $m^{-1}$ $K^{-1}$ and the heat loss coefficient is 20 W $m^{-2}$ $K^{-1}$

nodes in the axial and transverse directions, respectively. The simulations were performed on 2.4 GHz Pentium Xeon processors of 2 GB of RAM each.

A detailed description of the boundary conditions and calculation of transport properties can be found in previous work [21]. The exterior walls were modeled assuming Newton's law of cooling, as seen in Fig. A.1. A first-order kinetics model was employed along the catalytic wall. Given the lack of a reliable kinetic rate expression and the question of how generic is the behavior seen experimentally, a pre-exponential of $10^{13}$ $1\,s^{-1}$ and zero activation energy have been assumed. The latter choice gives self-ignition in the transient simulation. No attempt was made to fit the experimentally measured values (e.g., temperatures and times) by adjusting the kinetic and operating parameters.

The maximum temperature along the wall versus time was monitored for varying composition and flow rate to validate the assumptions made in deriving Eq. (1). Fig. A.2a and b shows the effect of composition at constant flow rate ($Q_{tot} = 1$ SLPM). As richer fuel content mixtures are used, the heat released from the catalytic combustion increases and thus both the steady state temperatures and heating rates increase. However, when the temperatures are normalized with the corresponding steady state temperatures, the transient trajectories collapse on each other. Fig. A.2c and d shows the effect of flow rate at fixed composition ($x_{MeOH} = 10\%$). As expected, the steady state temperature increases with increasing flow rate. In addition, the system reaches steady state faster at higher flow rates. These CFD results are qualitatively similar to the experimental observations, where only change in flow rate had a significant effect on the time to reach steady state.

## References

[1] C.K. Dyer, J. Power Sources 106 (2002) 31–34.
[2] A. Mitsos, I. Palou-Rivera, P.I. Barton, Ind. Eng. Chem. Res. 43 (2004) 74–84.
[3] J.D. Holladay, E.O. Jones, M. Phelps, J. Hu, J. Power Sources 108 (2002) 21–27.
[4] J.D. Holladay, J.S. Wainright, E.O. Jones, S.R. Gano, J. Power Sources 130 (2004) 111–118.
[5] S.K. Kamarudin, W.R.W. Daud, S.L. Ho, U.A. Hasran, J. Power Sources 163 (2007) 743–754.
[6] K.M. McGrath, G.K.S. Prakash, G.A. Olah, J. Ind. Eng. Chem. 10 (2004) 1063–1080.
[7] A.K. Avci, D.L. Trimm, Z.I. Onsan, Chem. Eng. J. 90 (2002) 77–87.
[8] D.G. Norton, E.D. Wetzel, D.G. Vlachos, Ind. Eng. Chem. Res. 45 (2006) 76–84.
[9] J.A. Federici, D.G. Norton, T. Bruggemann, K.W. Voit, E.D. Wetzel, D.G. Vlachos, J. Power Sources 161 (2006) 1469–1478.
[10] D.G. Norton, K.W. Voit, T. Brüggemann, E.D. Wetzel, D.G. Vlachos, Proceedings of the 24th Army Science Conference, Orlando, FL, 2004.
[11] W.M. Yang, S.K. Chou, C. Shu, Z.W. Li, H. Xue, Appl. Phys. Lett. 84 (2004) 3864–3866.
[12] C. Zhang, N. Najafi, L.P. Bernal, P.D. Washabaugh, Proceedings of the 12th International Conference on Solid-State Sensors, Actuators and Microsystems, Boston, MA, USA, 2003, pp. 40–44.
[13] D.G. Norton, D.G. Vlachos, Proc. Combust. Inst. 30 (2005) 2473–2480.
[14] B. Lindström, L.J. Pettersson, Chem. Eng. Technol. 26 (2003) 473–478.
[15] Z.Y. Hu, V. Boiadjiev, T. Thundat, Energy Fuels 19 (2005) 855–858.
[16] C.J. Jiang, D.L. Trimm, M.S. Wainwright, Chem. Eng. Technol. 18 (1995) 1–6.
[17] J.P. Brunelle, Pure Appl. Chem. 50 (1978) 1211–1229.
[18] G. Ertl, H. Knözinger, J. Weitkamp, Handbook of Heterogeneous Catalysis, VCH, Weinheim, 1997.
[19] G. McCullough, R. Douglas, S. Spence, G. Cunningham, Proc. Inst. Mech. Eng. Part D: J. Automob. Eng. 218 (2004) 229–241.
[20] K. Yoshida, S. Tanaka, S. Tomonari, D. Satoh, M. Esashi, J. Microelectromech. Syst. 15 (2006) 195–203.
[21] D.G. Norton, D.G. Vlachos, Chem. Eng. Sci. 58 (2003) 4871–4882.